ACS OMEGA

http://pubs.acs.org/journal/acsodf
Article

Boosting the Electrochemical Storage Properties of Co_3O_4 Nanowires by the Mn Doping Strategy with Appropriate Mn Doping Concentrations

Jun Wang, Huifang Zhang, Haoyan Duan, Heming Zhao,* Juncheng Qi, Boxiang Ma, and Honghui Fan

Cite This: *ACS Omega* 2024, 9, 6955–6964

Read Online

ACCESS | Metrics & More | Article Recommendations | Supporting Information

ABSTRACT: High specific capacitance, high energy density, and high power density have always been important directions for the improvement of electrode materials for supercapacitors. In this paper, Co_3O_4 nanowire arrays with various Mn doping concentrations (Mn:Co molar ratio = 1:11, 1:5, 1:2) directly grown on nickel foam (NF) were prepared by a simple hydrothermal method and annealing process. The influence of Mn doping on the morphology, structure, and electrochemical behaviors of Co_3O_4 was investigated. The results show that partial substitution of Co ions with Mn ions in the spinel structure does not change the nanowire morphology of pure Co_3O_4 but increases the lattice parameter and decreases the crystallinity of cobalt oxide. Electrochemical measurements showed that Mn doping in Co_3O_4 could effectively enhance the redox activity, especially Co_3O_4 with a Mn doping ratio of 1:5, which exhibits the most excellent electrochemical performance, with the maximum specific capacitance of 1210.8 $F \cdot g^{-1}$ at 1 $A \cdot g^{-1}$ and a rate capability of 33.0% at 30 $A \cdot g^{-1}$. The asymmetric supercapacitor (ASC) device assembled with the optimal Mn−Co_3O_4 (1:5) and activated carbon (AC) electrode performs a high specific capacitance of 105.8 $F \cdot g^{-1}$, a high energy density of 33 $Wh \cdot kg^{-1}$ at a power density of 748.1 $W \cdot kg^{-1}$, and a capacitance retention of 60.2% after 5000 cycles. This work indicates that an appropriate Mn doping concentration in the Co_3O_4 lattice structure will have great potential in rationalizing the design of spinel oxides for efficient electrochemical performance.

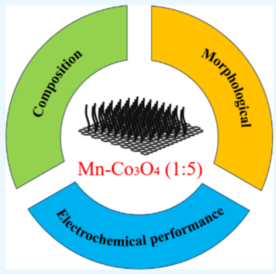

INTRODUCTION

Recently, with the rapid development of society, the rapid consumption of fossil energy, and the increasingly serious environmental pollution, human beings urgently need alternative new clean renewable energy.[1] The development of electrochemical energy storage devices is considered to be one of the most practical and efficient options.[2] Supercapacitors are a good choice for energy storage because of their advantages such as fast charge and discharge rate, high power density, and good cycle stability.[3] Electrode materials are one of the key factors determining the performance of supercapacitors. Co_3O_4 is a very important electrode material for supercapacitors because of its extremely high theoretical capacitance (3560 $F \cdot g^{-1}$), simple synthesis method, relatively low price, etc.[4,5] However, it is essentially a semiconductor with poor electrical conductivity, which greatly limits the rapid transmission of electrons and exhibits low capacitance values in practical applications.[6,7] Therefore, how to effectively improve its actual capacitance is still a problem worth studying.

In order to effectively solve this problem, carbon coating on Co_3O_4 is one of the most commonly used strategies.[8] Carbon coating can provide efficient electron and ion transport channels while forming a conductive network between the particles to accelerate the electron transfer rate and reduce the cell polarization; The porous structure of the carbon coating layer can absorb the electrolyte, thus increasing the contact area between the electrolyte and the active material and effectively improving the electrochemical performance of the material. However, this will bring additional contact resistance, as well as the problem that the coating layer of the composite is easy to fall off during repeated charging and discharging.[9]

The current improvement methods mainly focus on two aspects: First, the construction of nanostructures, such as nanoparticles,[10] nanowires,[11] nanorods,[12] and nanosheets,[13] which can greatly improve the contact area between electrode materials and electrolyte promotes redox reaction and then improves the specific capacitance. Second is to directly grow the material on the three-dimensional conductive matrix (such as nickel foam or graphene sheet[14]) to build a binder-free electrode, which is conducive to the high affinity between the active material and the current collector, improves the conductivity of the overall integrated electrode, and reduces the inherent resistance of the active electrode material.[15−20] However, the use of these methods to improve the conductivity is very limited. Recent studies have shown that electrode materials mainly determine the final electrochemical properties of supercapacitors.[21−26] The method of bulk phase

Received: November 1, 2023
Revised: January 11, 2024
Accepted: January 17, 2024
Published: February 2, 2024

https://doi.org/10.1021/acsomega.3c08650
ACS Omega 2024, 9, 6955−6964

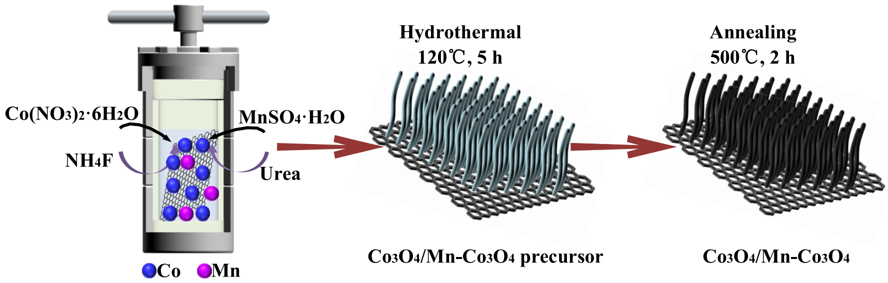

Figure 1. Schematic of the synthesis process of the Co_3O_4 and Mn−Co_3O_4 on nickel foam.

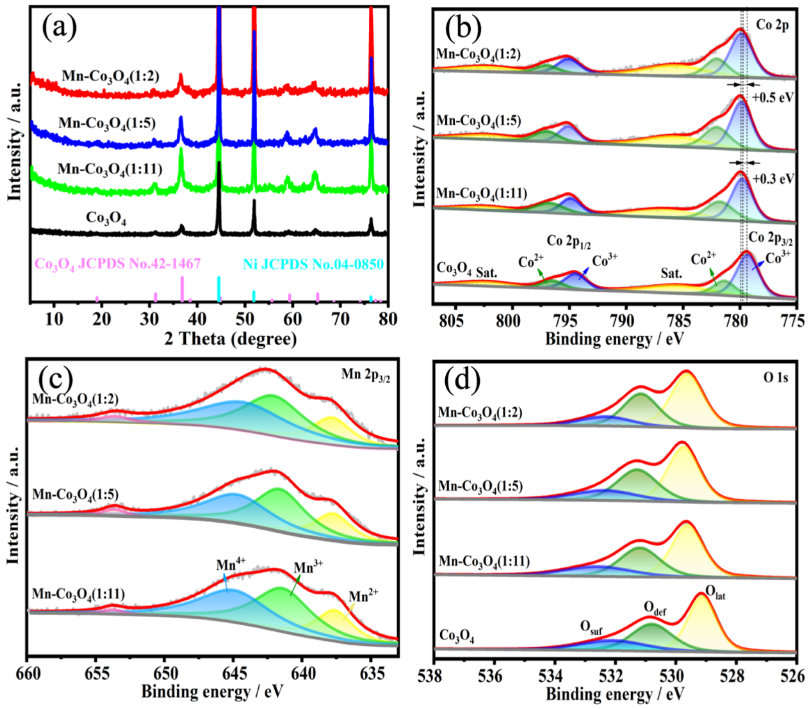

Figure 2. (a) XRD patterns. XPS spectra of the as-prepared Co_3O_4 and Mn−Co_3O_4 with different molar ratios of (b) Co 2p, (c) Mn 2p, and (d) O 1s.

doping can solve this problem effectively.[27−29] For example, Alem et al.[30] prepared Ag-doped Co_3O_4 nanoparticles (NPs) with different concentrations by coprecipitation, exhibiting a specific capacitance value of 992.7 $F·g^{-1}$ at a scanning rate of 5 $mV·s^{-1}$ and energy and power densities of 27.9 $Wh·kg^{-1}$ and 3816.1 $W·kg^{-1}$, respectively. Hassan et al.[31] studied the electrochemical properties of Zn doped with different concentrations FTO/Co_3O_4:Zn prepared by the spray pyrolysis technique, with a maximum area capacitance of 5.37 $mF·cm^{-2}$, and explained the reason for its better charge storage performance through Nyquist plots. All of these are attributed to doping-induced electron transfer and significant electron modulation, resulting in improved catalytic, optical, magnetic, chemical, and physical properties. However, the preparation methods of these electrode materials are expensive, require complex instruments, and take a relatively long time to prepare.[32,33]

In this paper, a nickel foam with strong durability and excellent conductivity was selected as the conductive matrix, and Co_3O_4 electrode materials with different Mn doping concentrations were grown on the nickel foam substrate by a simple hydrothermal and annealing method. The phase and morphology of the synthesized electrode materials were characterized by X-ray diffraction (XRD), X-ray photoelectron spectroscopy (XPS), scanning electron microscopy (SEM), and transmission electron microscopy (TEM). The electrochemical properties were compared by galvanostatic charge−discharge (GCD), cyclic voltammetry (CV), and electrochemical impedance spectroscopy (EIS). The optimal Mn−Co_3O_4/NF with a Mn:Co molar ratio of 1:5 and AC is selected to assemble an asymmetric supercapacitor, which has a high energy density (33 $Wh·kg^{-1}$) and power density (748.1 $W·kg^{-1}$), as well as a good cycle stability of 60.2% after 5000 cycles.

■ EXPERIMENTAL SECTION

Material Synthesis. *Nickel Foam Treatment.* The nickel foam is cut into a rectangle shape of 2 cm × 3 cm and cleaned with hydrochloric acid and acetone in the ultrasonic cleaning machine to remove the oxides on its surface. After that, the residual impurities on the surface are thoroughly cleaned with deionized (DI) water and ethanol and dried in an electric thermostatic drying oven at 50 °C for 24 h.

Sample Preparation. The synthesis process of Co_3O_4 and Mn-doped Co_3O_4 is shown in Figure 1. Co $(NO_3)_2·6H_2O$, $MnSO_4·H_2O$, and urea were added to 45 mL of DI water,

https://doi.org/10.1021/acsomega.3c08650
ACS Omega 2024, 9, 6955−6964

Table 1. XPS Spectral Data of Different Forms of Mn, Co, and O of Co_3O_4 and Different Mn-Doped Co_3O_4

samples	Co^{2+}	Co^{3+}	Mn^{2+}	Mn^{3+}	Mn^{4+}	O_l	O_d	O_s
Co_3O_4	28.3%	71.7%				47%	33%	20%
Mn−Co_3O_4 (1:11)	38%	62%	18.8%	41.7%	39.5%	46.9%	33.7%	19.4%
Mn−Co_3O_4 (1:5)	39.8%	60.2%	17.8%	40.6%	41.6%	45.2%	34.8%	20%
Mn−Co_3O_4 (1:2)	31%	69%	20%	42.5%	37.5%	47%	33.7%	19.2%

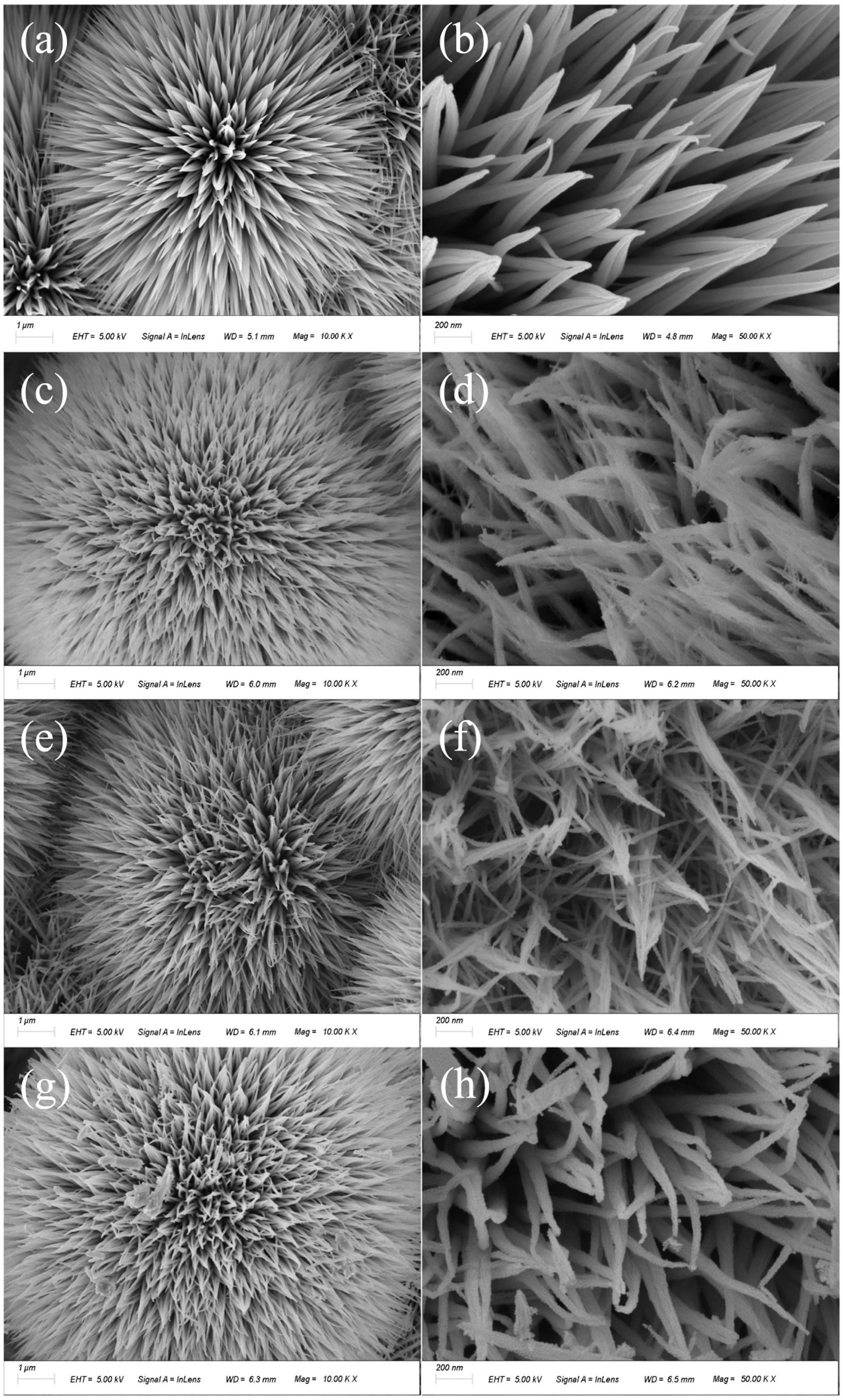

Figure 3. SEM images of (a, b) Co_3O_4, (c, d) Mn−Co_3O_4 (1:11), (e, f) Mn−Co_3O_4 (1:5), and (g, h) Mn-Co_3O_4 (1:2).

respectively, and stirred at room temperature for 30 min to completely dissolve them. Finally, NH_4F was added to the solution and stirred for 30 min. The obtained solution was transferred to a 50 mL Teflon-lined autoclave, and the treated nickel foam was vertically inserted into the autoclave. A 5 h hydrothermal reaction was performed in an electric thermostatic drying oven at 120 °C, and then the nickel foam was taken out, soaked in DI water and ethanol, shaken and washed six times, and dried at 50 °C for 10 h. In a tube furnace, the annealing was carried out at 500 °C for 2 h at a heating rate of

https://doi.org/10.1021/acsomega.3c08650
ACS Omega 2024, 9, 6955−6964

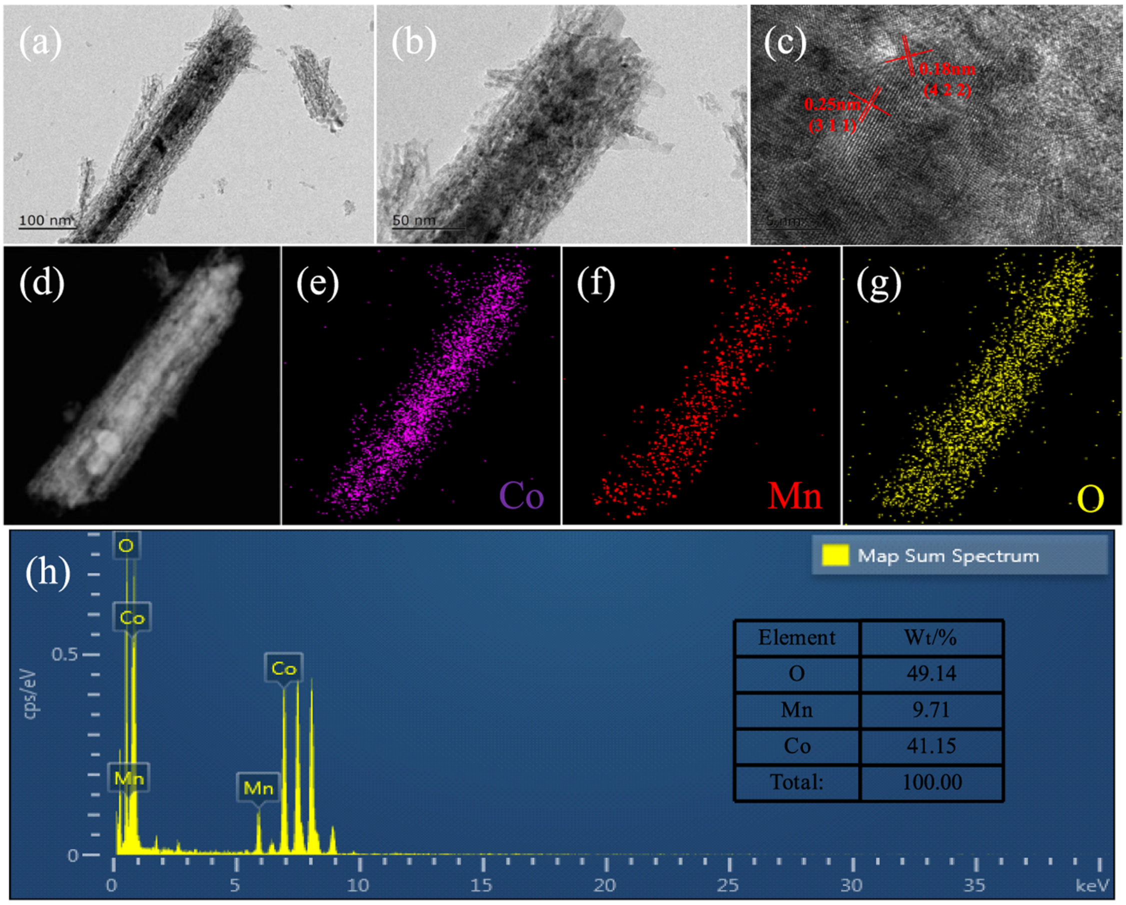

Figure 4. (a–c) TEM and HRTEM images of Mn–Co_3O_4 (1:5). (d) EDS mapping images and presence of (e) Co, (f) Mn, and (g) O. (h) EDS spectrum of Mn–Co_3O_4 (1:5).

5 °C·min^{-1}. The total dosage of Co $(NO_3)_2{\cdot}6H_2O$ and $MnSO_4{\cdot}H_2O$ is 2 mmol, and the doping ratio was achieved by changing the dosage of $MnSO_4{\cdot}H_2O$:Co $(NO_3)_2{\cdot}6H_2O$ (0:1, 1:11, 1:5, and 1:2). The obtained samples are named Co_3O_4/NF, Mn–Co_3O_4 (1:11)/NF, Mn–Co_3O_4 (1:5)/NF, and Mn–Co_3O_4 (1:2)/NF, respectively.

Materials Characterization. The prepared samples were characterized as follows. The XRD (Bruker D8 ADVANCE X-ray diffractometer with Cu Kα) test was performed at a scanning rate of 4°·min^{-1} in the range of 5–80°. SEM (ZEISS Sigma 300) and TEM (JEM 2100F) with EDX were used to characterize the sample morphology and element content. XPS (Thermo Scientific K-Alpha) was performed for composition analysis, chemical binding, oxidation state calculation, and binding energy analysis.

Electrochemical Performance Test. The electrochemical properties of the prepared electrodes were studied by an electrochemical workstation (Chenhua, CHI760E). In the conventional three-electrode system, the sample was used as the working electrode, Pt as the counter electrode, and Hg/HgO as the reference electrode, respectively. In addition, we also assembled an ASC with Mn–Co_3O_4 (1:5)/NF as the positive electrode and AC as the negative electrode. AC electrodes were prepared by mixing AC powder, acetylene black, and polytetrafluoroethylene (PTFE) in ethanol at a ratio of 8:1:1 and coated on nickel foam. The electrolyte of all experiments was a 3 M KOH solution. In order to analyze the electrochemical performance of the material, CV was performed at a scanning rate of 1–30 mV s^{-1}, GCD was performed at a current density of 1–10 A·g^{-1}, and EIS testing was performed at an amplitude of 5 mV in the frequency range of 0.01 to 100,000 Hz, respectively.

■ RESULTS AND DISCUSSION

The phase purity and crystal structure of pure Co_3O_4 and Co_3O_4 doped with different Mn concentrations were characterized by XRD. Figure 2a shows the XRD pattern of the as-prepared samples, which is basically similar to that of standard Co_3O_4 (JCPDS No. 42-1467), and no new diffraction peaks appear, indicating that no new crystal phase appears after doping.[34] The three strongest diffraction peaks correspond to Ni in the conductive matrix nickel foam (JCPDS No. 04-0850). With the increase of the Mn doping ratio, the crystallinity of the sample shows a decreasing trend, indicating that a large amount of Mn doping may cause the crystal structure of Co_3O_4 to become unstable. At the same time, the peak shifts toward a lower diffraction angle. This is because the atomic radius of Mn (0.68 Å) is generally larger than that of Co (0.65 Å), and when Mn partially replaces Co in the Co_3O_4 lattice, both the lattice constant and the plane spacing (d) are larger than the original values. Therefore, according to Bragg equation, the diffraction peak of Co_3O_4 has a certain degree of negative shift,[35] which also indicates the existence of Mn and Co oxide coordination.

The spectra of Co 2p, Mn 2p, and O 1s in Co_3O_4 and Mn–Co_3O_4 were used to analyze the composition and structure of

https://doi.org/10.1021/acsomega.3c08650
ACS Omega 2024, 9, 6955–6964

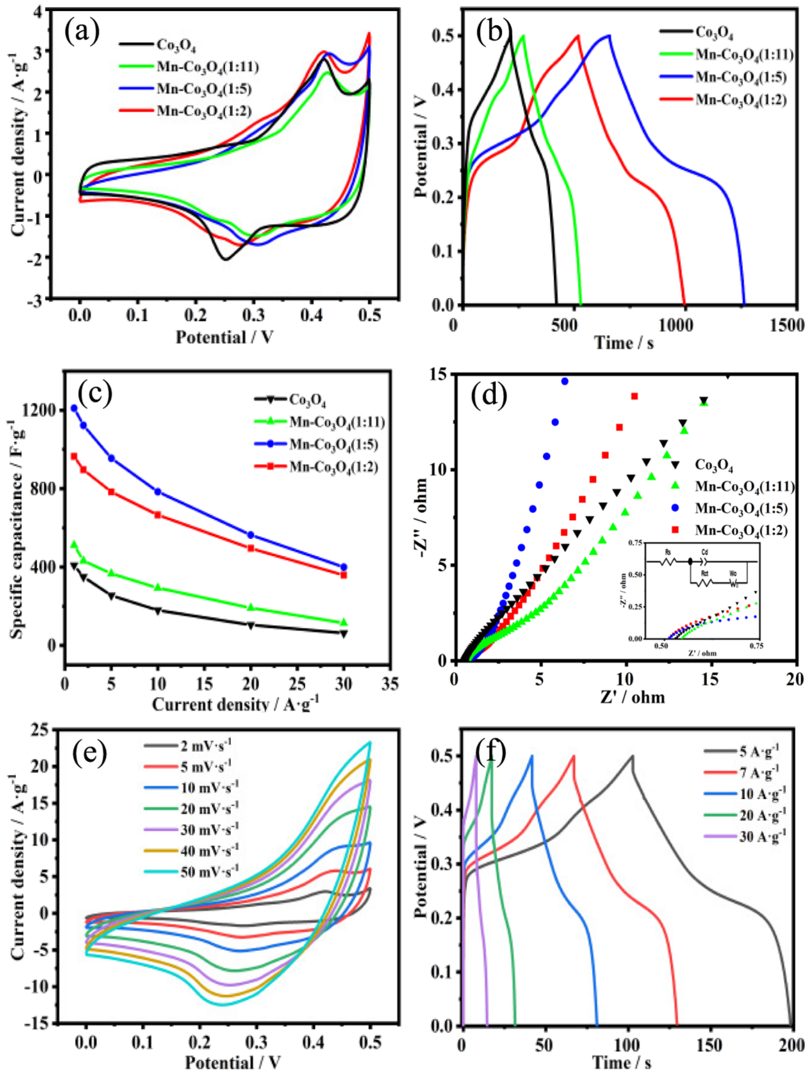

Figure 5. Electrochemical performance of Co_3O_4/NF and Mn−Co_3O_4/NF with different Mn/Co molar ratios. (a) CV curves at a scan rate of 1 mV·s^{-1}. (b) GCD curves at a current density of 1 A·g^{-1}. (c) Specific capacitances at different current densities. (d) EIS curves and the equivalent circuit model. (e) CV curves at different scan rates. (f) GCD curves at different current densities of Mn−Co_3O_4 (1:5)/NF.

the samples (Figure 2b−d). Figure 2b shows the XPS spectra of Co 2p under different Mn doping ratios. From the Co 2p spectra of Co_3O_4 samples, it can be seen that the peaks of binding energy at 779.3 and 794.5 eV belong to Co^{3+} while the peaks at 781.4 and 796.5 eV correspond to Co^{2+}. The two satellite peaks of the sample are located at 785.5 and 802.3 eV, respectively. In addition, with the increase of Mn doping ratio, the positive shift amplitude of binding energy at positions of Co^{3+} and Co^{2+} and their satellite peaks in the sample also increase accordingly. The reason for this positive shift is that the doping of Mn leads to electron transfer and modulation,[36,37] which also proves that different contents of Mn are successfully doped.

Figure 2c shows the XPS spectra of Mn $2p_{3/2}$ at different Mn doping ratios. It can be seen that peaks near 644.7, 641.6, and 637.7 eV belong to Mn^{4+}, Mn^{3+}, and Mn^{2+}, respectively.[38] With the increase of the Mn content in the sample, the peak intensity of Mn $2p_{3/2}$ in the sample increases. Meanwhile, it can be seen that the relative area of the characteristic peak of Mn^{4+} is always higher than that of Mn^{2+}, which makes the mixed sample in a stable state.[39,40]

As shown in Figure 2d, the XPS spectra of O 1s of the samples exhibit three peaks near 529.5, 531.1, and 532.2 eV, respectively, originating from lattice oxygen, oxygen defect, and adsorbed oxygen.[41−44] It can be seen that the ratio of oxygen defects increases when Mn is doped in Co_3O_4. This is because replacing Co^{3+} with Mn^{2+} may cause oxygen vacancies, resulting in the formation of more oxygen defects.[45] Oxygen vacancies can promote ion transport and electron conduction, leading to better electrochemical performance.[39]

We have listed the XPS spectrum data of different forms of Mn, Co, and O (Table 1). It can be seen from the table that Mn^{4+} ions occupy the largest proportion in Mn−Co_3O_4, which further indicates that Mn doping makes the sample more stable. The proportion of O_d and O_s increases, thus providing more active sites for REDOX reactions and resulting in improved electrochemical performance. This is consistent with the results of XPS analysis.

The morphology of the prepared pure Co_3O_4 and Mn-doped Co_3O_4 was analyzed by SEM (Figure 3); it can be seen that the smooth nickel foam was covered with dense nanostructured surface nanowires. The nanowires are uniformly arranged on the nickel foam, and there are many spaces between these nanowires. The enlarged SEM images show that the morphology of the nanowires remains basically unchanged when Mn is doped into a Co_3O_4 spinel structure, and the morphology of Mn−Co_3O_4 (1:5) nanowires becomes thinner and denser compared with pure Co_3O_4 and other Mn-doped Co_3O_4 samples.

As shown in Figure 4a−c, TEM and HRTEM images were provided to further investigate the morphology and microstructure of Mn−Co_3O_4 (1:5). Figure 4a shows a typical nanowire morphology of Mn−Co_3O_4 (1:5), which is consistent with SEM. Figure 4b shows that there are numerous pores inside the nanowires, which can expose more active sites for electrochemical reactions. The pores are caused by inorganic conversion during heat treatment and the release of gas molecules.[36] The formation of nanowire, high porosity, and a denser nanowire array structure make ions easier to transport during charge and discharge, increase the active surface area to a certain extent, and thus provide a large number of active sites for redox reactions, so appropriate Mn doping is expected to improve electrochemical performance.[46]

HRTEM (Figure 4c) clearly shows the presence of two sets of lattice fringes with lattice spacings of 0.18 and 0.25 nm, corresponding to (422) and (311) of Co_3O_4, respectively. Their values are larger than the theoretical values of 0.17 nm (422) and 0.24 nm (311) for the lattice spacing of the corresponding planes of Co_3O_4. It is further proved that Mn with a larger radius is successfully doped into the crystal structure of Co_3O_4, which is consistent with XRD results. Figure 4 shows that Mn-doped Co_3O_4 nanowires have three elements, Co (Figure 4e), Mn (Figure 4f), and O (Figure 4g), which are evenly distributed on the nickel foam, confirming the purity of the material. Combined with previous XRD and XPS analyses, Mn was successfully doped into Co_3O_4. The contents of Co, Mn, and O elements (Figure 4h) are 41.15, 9.71, and 49.14%, respectively, which are close to the molar ratios of theoretical manganese and cobalt elements.

To evaluate the electrochemical behaviors of as-prepared Co_3O_4/NF and Mn−Co_3O_4/NF with different Mn doping concentrations as electrode materials for supercapacitors, we performed CV, GCD, and EIS tests in a 3 M KOH electrolyte. Figure 5a shows the CV curves of Co_3O_4/NF and Mn−Co_3O_4/NF electrodes with different Mn doping concentrations in a potential window of 0−0.5 V at a scanning rate of 1 $mV·s^{-1}$. Obviously, the shape of CV curves after Mn doping has almost no change, indicating that they have the same electrochemical energy storage mechanism.[47] All CV curves have two redox peaks corresponding to the reversible redox reactions of Co^{2+}/Co^{3+} and Co^{3+}/Co^{4+} with OH^- in the electrolyte,[48,49] indicating the pseudocapacitive behavior of the electrode material. The redox peaks are basically consistent with the voltage plateau in the GCD curve. With Mn doping, the integral area of the CV curve increases, which corresponds to the specific capacitance value. The distance between the oxidation peak and the reduction peak of Mn−Co_3O_4 is reduced as compared to pure Co_3O_4, indicating that Mn doping reduces the polarization due to the increase in electrical conductivity, which is consistent with the results discussed in EIS.

To further investigate their electrochemical properties, GCD tests of the Co_3O_4/NF and Mn−Co_3O_4/NF electrodes were performed at a potential window of 0−0.5 V at a current density of 1 $A·g^{-1}$. The GCD curve (Figure 5b) shows that in the potential window range of 0−0.5 V, all charge and discharge curves show nonlinear characteristics and the pseudocapacitance characteristics are reflected in combination with the voltage platform on the GCD curve.[50] These voltage platforms on the GCD curve are mainly caused by reversible redox reactions on the surface of electrode material,[51] and these voltage platforms coincide with the peak positions on the CV curve, respectively. This agrees well with the CV curve in Figure 5a. The specific capacitance of the electrode material can be calculated according to the GCD curve by eq 1:

$$C_s = \frac{I \times \Delta t}{m \times \Delta V} \quad (1)$$

where C_s is the specific capacitance ($F·g^{-1}$) of the electrode material, I is the discharge current (A), Δt is the discharge time (s), and m is the mass of the active material in the electrode (g). The specific capacitance at the current densities of 1, 2, 5, 10, 20, and 30 $A·g^{-1}$ was calculated (Figure 5c). As the current density increased, the specific capacitance of each electrode gradually decreased. However, the Mn−Co_3O_4 (1:5)/NF electrode exhibits a higher specific capacitance than other electrodes at all current densities, with a specific capacitance as high as 1210.8 $F·g^{-1}$ at 1 $A·g^{-1}$ and a rate capability of 33.0% at 30 $A·g^{-1}$. According to SEM and TEM results, this may be due to the fact that the dense nanowires and pore structures provide more active sites and larger contact surfaces for redox reactions, thus promoting electrochemical reactions and amplifying specific capacitance. The capacitance value is higher than other Mn-doped Co_3O_4 electrode materials previously studied. For example, Ambare et al.[52] used spray pyrolysis to deposit Mn on the surface of stainless steel. The specific capacitance of the obtained Mn:Co_3O_4 film can reach 485.2 $F·g^{-1}$ at 1 $mV·s^{-1}$, and it retained 73.58 $F·g^{-1}$ at 100 $mV·s^{-1}$. Karthikeyan and Mariappan[53] prepared Co_3O_4 NPs doped with different concentrations of Mn by the coprecipitation method. Co_3O_4: 7% Mn had a specific capacitance of 318 $F·g^{-1}$ at 5 $mV·s^{-1}$ and 80 $F·g^{-1}$ at 100 $mV·s^{-1}$. Aslam et al.[54] prepared Mn-doped Co_3O_4:$Mn_{0.05}Co_{2.95}O_4$ by the sol−gel auto combustion method, which can reach a specific capacitance of 81.8 $F·g^{-1}$ at 1 $A·g^{-1}$.

Information about different forms of resistance of Co_3O_4/NF and Mn−Co_3O_4/NF electrodes with different Mn doping concentrations was determined by using EIS. Figure 5d shows the EIS results in the frequency range of 0.1 Hz−100 kHz. In the high-frequency region, the intersection point with the real axis and the diameter of the semicircle are related to the resistance of the solution (including the inherent resistance of the electrode sheet, the contact resistance between the electrode and the nickel foam, and the ionic resistance of the electrolyte) and the charge transfer resistance (R_{ct}), respectively.[55] The slope of the EIS curve of Mn−Co_3O_4 (1:5)/NF is the largest in the low-frequency region, and the slope of Co_3O_4 is the smallest. From the equivalent circuit model (Figure 5d), it can be seen that the equivalent series resistance R_s of the Mn−Co_3O_4 (1:5)/NF electrode is 0.52 Ω and the charge transfer resistance R_{ct} is 0.1 Ω, which can be attributed to the improved conductivity provided by Mn doping. Moreover, Mn−Co_3O_4 (1:5)/NF has the steepest slope at low frequencies, indicating a faster ion diffusion rate. These characteristics suggest that Mn−Co_3O_4 (1:5)/NF can be used as an excellent electrode material.

Overall comparison, we believe that Mn−Co_3O_4 (1:5)/NF has better electrochemical performance. The improvement in electrochemical performance can be attributed to binder-free

https://doi.org/10.1021/acsomega.3c08650
ACS Omega 2024, 9, 6955−6964

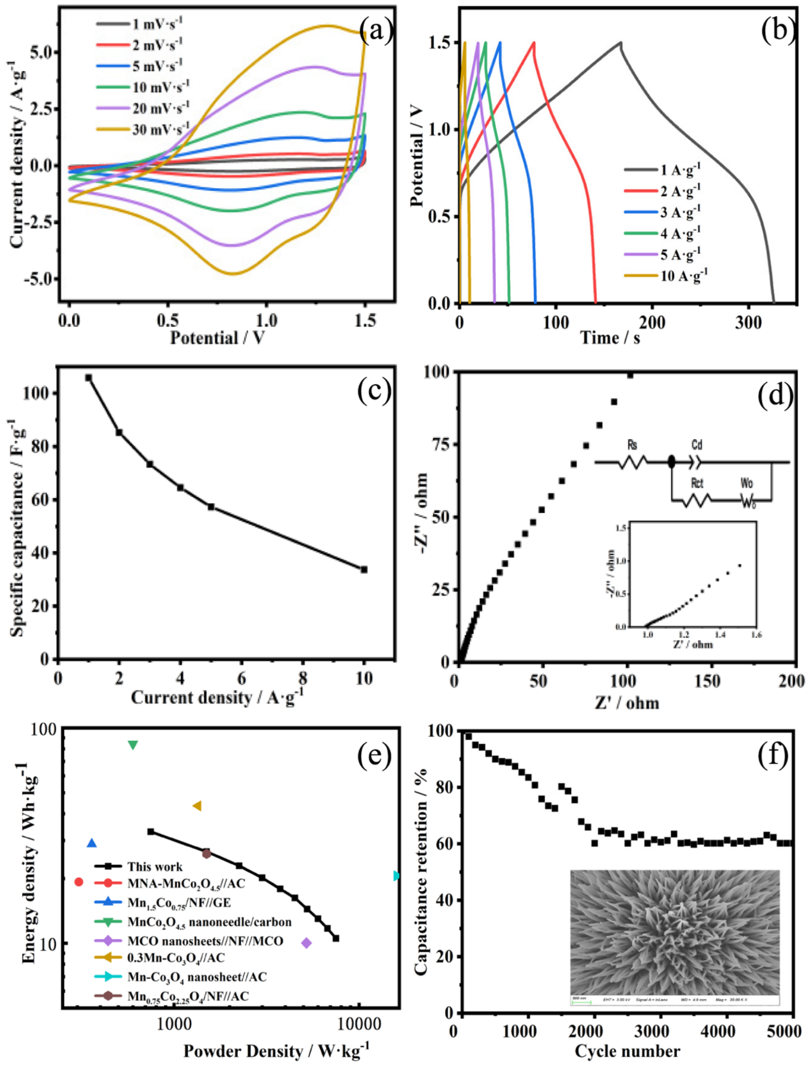

Figure 6. Electrochemical performances of $Mn-Co_3O_4$ (1:5)/NF//AC asymmetric supercapacitors. (a) CV curves. (b) GCD curves. (c) Specific capacitances at different current densities. (d) EIS curves with equivalent circuit. (e) Ragone plot. (f) 5000 charge and discharge cycles at a current density of 2 $A\cdot g^{-1}$, and the inset is the SEM image of the sample after 5000 cycles.

conditions and the appropriate amount of Mn doping, which promotes fast charge transfer. The surface of nickel foam has mechanically stable nanowire arrays with a porous structure, which can provide more active sites for ion adsorption and ion redox reaction and shorten the diffusion path of ions and electrons.[46]

Figure 5e shows the CV curve of $Mn-Co_3O_4$ (1:5)/NF at 2−50 $mV\cdot s^{-1}$. With the increase of scanning rate, the anode peak continuously moves to the direction of high potential and the cathode peak continuously moves to the direction of low potential. This may be due to the polarization effect and internal resistance in the Faraday redox reaction. Moreover, this peak shift indicates that the redox reaction is reversible and rapid and occurs between the electrolyte and the electrode.[56] Figure 5f shows the GCD curve at a current density of 5−30 $A\cdot g^{-1}$. It can be observed that as the current density increases, the specific capacitance decreases. This is because when a lower current density is applied, enough ions of the electrolyte will creep into the electrode, thus increasing the likelihood of a redox reaction between the electrolyte and the electrode.[57]

In order to further explore the practical application of the $Mn-Co_3O_4$ (1:5)/NF electrode, ASC devices with $Mn-Co_3O_4$ (1:5)/NF as the positive electrode and AC as the negative electrode were assembled. Figure 6a shows the CV curves at different scanning rates; with the increase of scanning rate, the shape of the CV curve remains unchanged, indicating that it has excellent rate capacitance and reversibility. The GCD curve under different current densities (Figure 6b) shows good symmetry. According to formula 1, when the current densities are 1, 2, 3, 4, 5, and 10 $A\cdot g^{-1}$, the specific capacitances are 105.9, 85.3, 73.4, 64.5, 57.3, and 33.7 $F\cdot g^{-1}$, respectively (as shown in Figure 6c). This shows that the assembled ASC has a good capacitance and rate performance. Figure 6d shows the EIS curve and its equivalent circuit of the ASC device. The internal resistance R_S is 1.0 Ω, indicating that it has a very low internal resistance. 5000 consecutive GCD tests were conducted under 2 $A\cdot g^{-1}$ to evaluate its cycle performance (Figure 6f). In the first 2000 cycles, the capacitance retention can reach 60.2% and remained almost stable in the subsequent 3000 cycles, according to the SEM image after 5000 cycles (Figure 6f inset), it can be seen that the nanowire morphology of the $Mn-Co_3O_4$ (1:5)/NF remains but the pseudocapacitance behavior results in the thickening of the nanowires; this may be caused by the

https://doi.org/10.1021/acsomega.3c08650
ACS Omega 2024, 9, 6955−6964

accumulation of active substances on the electrode surface during charging and discharging. However, after 2000 cycles, its capacity remained the same, proving its usefulness in high-performance SC devices. Binder-free and porous topography provides excellent electrical connectivity.

The energy density and power density of the assembled ASC device can be calculated from specific capacitance and discharge time according to eqs 2 and 3.

$$E = \frac{C \times \Delta V^2}{2 \times 3.6} \quad (2)$$

$$P = \frac{3600 \times E}{\Delta t} \quad (3)$$

where E is the energy density (Wh·kg^{-1}), C is the specific capacitance (F·g^{-1}), ΔV is the voltage window (V), P is the power density (W·kg^{-1}), and Δt is the discharge time (s). The Ragone diagram of Figure 6e shows that the energy density of the ASC device can reach 33 Wh·kg^{-1} under the power density of 748.1 W·kg^{-1}. Due to the reasonable matching of the two electrodes, the energy density of the assembled ASC device is much higher than that of most similar devices, such as MNA-$MnCo_2O_{4.5}$//AC (19.3 Wh·kg $^{-1}$, 306 W·kg $^{-1}$),[43] $Mn_{1.5}Co_{0.75}$/NF//GE (25.88 Wh·kg $^{-1}$, 359.5 W·kg^{-1}),[46] $MnCo_2O_{4.5}$ nanoneedle/carbon (84.3 Wh·kg $^{-1}$, 600 W·kg^{-1}),[58] 0.3Mn−Co_3O_4//AC (43.5 Wh·kg $^{-1}$, 1350 W·kg^{-1}),[40] Mn−Co_3O_4 nanosheet//AC (20.6 Wh·kg $^{-1}$, 16000 W·kg^{-1}),[59] $Mn_{0.75}Co_{2.25}O_4$/NF//AC (1500 Wh·kg $^{-1}$, 26.04 W·kg^{-1}),[60] and MCO nanosheets//NF//MCO (10.04 Wh·kg^{-1}, 5200 W·kg^{-1}).[16]

■ CONCLUSIONS

In a nutshell, we provide a simple method to synthesize Mn-doped Co_3O_4 nanowires with different concentrations and the successful doping of Mn is proven by XRD, XPS, and EDS. After that, the morphology was analyzed by SEM and TEM. The electrochemical properties were analyzed in a three-electrode system. The results show that the Mn−Co_3O_4 (1:5)/NF electrode has the best electrochemical performance. This excellent electrochemical performance can be attributed to the fine-tuning of the structure by an appropriate amount of Mn doping, where the denser and more porous structure provides more active sites for redox reaction and promotes rapid charge transfer; the binder-free electrode with nickel foam as the conductive matrix reduces the intrinsic resistance of the electrode material and provides excellent electrical connectivity. In addition, the prepared samples maintained satisfactory energy density and power density after being assembled into an ASC device. This indicates that the prepared materials are promising electrode materials for energy storage devices.

■ ASSOCIATED CONTENT

Supporting Information

The Supporting Information is available free of charge at https://pubs.acs.org/doi/10.1021/acsomega.3c08650.

Electrochemical performance of the AC negative electrode (S1) (PDF)

■ AUTHOR INFORMATION

Corresponding Author

Heming Zhao − *College of Mechatronics Engineering, North University of China, Taiyuan 030051, P. R. China;* orcid.org/0000-0001-8933-8048; Email: zhm@nuc.edu.cn

Authors

Jun Wang − *College of Mechatronics Engineering, North University of China, Taiyuan 030051, P. R. China;* orcid.org/0009-0007-3859-064X

Huifang Zhang − *College of Mechatronics Engineering, North University of China, Taiyuan 030051, P. R. China;* orcid.org/0000-0001-6920-4069

Haoyan Duan − *China North Standardization Center, Beijing 100089, P.R. China*

Juncheng Qi − *School of Information and Communication Engineering, North University of China, Taiyuan 030051, P. R. China*

Boxiang Ma − *College of Mechatronics Engineering, North University of China, Taiyuan 030051, P. R. China*

Honghui Fan − *College of Mechatronics Engineering, North University of China, Taiyuan 030051, P. R. China*

Complete contact information is available at: https://pubs.acs.org/10.1021/acsomega.3c08650

Notes

The authors declare no competing financial interest.

■ ACKNOWLEDGMENTS

This work was financially supported by the National Natural Science Foundation of China under grant number 62201522 and the Fundamental Research Program of Shanxi Province under grant number 202203021212157.

■ REFERENCES

(1) Liu, S.; Kang, L.; Jun, S. C. Challenges and Strategies toward Cathode Materials for Rechargeable Potassium-Ion Batteries. *Adv. Mater.* **2021**, *33* (47), No. e2004689.

(2) Zhang, Y.; Zhou, C.-G.; Yang, J.; Xue, S.-c.; Gao, H.-l.; Yan, X.-h.; Huo, Q.-y.; Wang, S.-w.; Cao, Y.; Yan, J. Advances and challenges in improvement of the electrochemical performance for lead-acid batteries: A comprehensive review. *J. Power Sources* **2022**, *520*, No. 230800.

(3) Qiu, Q.; Zhu, M. M.; Li, Z. L.; Qiu, K. L.; Liu, X. Y.; Yu, J. Y.; Ding, B. Highly flexible, breathable, tailorable and washable power generation fabrics for wearable electronics. *Nano Energy* **2019**, *58*, 750−758.

(4) Xiao, Y.; Liu, S.; Li, F.; Zhang, A.; Zhao, J.; Fang, S.; Jia, D. 3D Hierarchical Co_3O_4 Twin-Spheres with an Urchin-Like Structure: Large-Scale Synthesis, Multistep-Splitting Growth, and Electrochemical Pseudocapacitors. *Adv. Funct. Mater.* **2012**, *22* (19), 4052−4059.

(5) Ding, K.; Yang, P.; Hou, P.; Song, X.; Wei, T.; Cao, Y.; Cheng, X. Ultrathin and Highly Crystalline Co_3O_4 Nanosheets In Situ Grown on Graphene toward Enhanced supercapacitor Performance. *Adv. Mater. Interfaces* **2017**, *4* (3), 1600884.

(6) Shi, Z.; Xing, L.; Liu, Y.; Gao, Y.; Liu, J. A porous biomass-based sandwich-structured Co_3O_4@Carbon Fiber@Co_3O_4 composite for high-performance supercapacitors. *Carbon* **2018**, *129*, 819−825.

(7) Isho, R. D.; Sher Mohammad, N. M.; Omer, K. M. Enhancing enzymatic activity of Mn@Co_3O_4 nanosheets as mimetic nanozyme for colorimetric assay of ascorbic acid. *Anal. Biochem.* **2022**, *654*, No. 114818.

(8) Salunkhe, R. R.; Tang, J.; Kamachi, Y.; Nakato, T.; Kim, J. H.; Yamauchi, Y. Asymmetric Supercapacitors Using 3D Nanoporous Carbon and Cobalt Oxide Electrodes Synthesized from a Single Metal-Organic Framework. *ACS Nano* **2015**, *9* (6), 6288−6296.

(9) Liu, S.; Kang, L.; Henzie, J.; Zhang, J.; Ha, J.; Amin, M. A.; Hossain, M. S. A.; Jun, S. C.; Yamauchi, Y. Recent Advances and

Perspectives of Battery-Type Anode Materials for Potassium Ion Storage. *ACS Nano* **2021**, *15* (12), 18931−18973.
(10) Vijayakumar, S.; Ponnalagi, A. K.; Nagamuthu, S.; Muralidharan, G. Microwave assisted synthesis of Co_3O_4 nanoparticles for high-performance supercapacitors. *Electrochim. Acta* **2013**, *106*, 500−505.
(11) Xia, X.-h.; Tu, J.-p.; Mai, Y.-j.; Wang, X.-l.; Gu, C.-d.; Zhao, X.-b. Self-supported hydrothermal synthesized hollow Co_3O_4 nanowire arrays with high supercapacitor capacitance. *J. Mater. Chem.* **2011**, *21* (25), 9319−9325.
(12) Wang, G. X.; Shen, X. P.; Horvat, J.; Wang, B.; Liu, H.; Wexler, D.; Yao, J. Hydrothermal Synthesis and Optical, Magnetic, and Supercapacitance Properties of Nanoporous Cobalt Oxide Nanorods. *J. Phys. Chem. C* **2009**, *113* (11), 4357−4361.
(13) Meher, S. K.; Rao, G. R. Ultralayered Co_3O_4 for High-Performance supercapacitor Applications. *J. Phys. Chem. C* **2011**, *115* (31), 15646−15654.
(14) Xiang, C. C.; Li, M.; Zhi, M. J.; Manivannan, A.; Wu, N. Q. A reduced graphene oxide/Co_3O_4 composite for supercapacitor electrode. *J. Power Sources* **2013**, *226*, 65−70.
(15) Ansari, S. A.; Khan, N. A.; Hasan, Z.; Shaikh, A. A.; Ferdousi, F. K.; Barai, H. R.; Lopa, N. S.; Rahman, M. M. Electrochemical synthesis of titanium nitride nanoparticles onto titanium foil for electrochemical supercapacitors with ultrafast charge/discharge. *Sustainable Energy & Fuels* **2020**, *4* (5), 2480−2490.
(16) Sahoo, S.; Naik, K. K.; Rout, C. S. Electrodeposition of spinel $MnCo_2O_4$ nanosheets for supercapacitor applications. *Nanotechnology* **2015**, *26* (45), No. 455401.
(17) Burke, M.; Larrigy, C.; Vaughan, E.; Paterakis, G.; Sygellou, L.; Quinn, A. J.; Herzog, G.; Galiotis, C.; Iacopino, D. Fabrication and Electrochemical Properties of Three-Dimensional (3D) Porous Graphitic and Graphenelike Electrodes Obtained by Low-Cost Direct Laser Writing Methods. *Acs Omega* **2020**, *5* (3), 1540−1548.
(18) Roy, A.; Jadhav, H. S.; Thorat, G. M.; Seo, J. G. Electrochemical growth of $Co(OH)_2$ nanoflakes on Ni foam for methanol electro-oxidation. *New J. Chem.* **2017**, *41* (17), 9546−9553.
(19) Chodankar, N. R.; Dubal, D. P.; Ji, S. H.; Kim, D. H. Superfast Electrodeposition of Newly Developed $RuCo_2O_4$ Nanobelts over Low-Cost Stainless Steel Mesh for High-Performance Aqueous supercapacitor. *Adv. Mater. Interfaces* **2018**, *5* (15), 1800283.
(20) Maile, N. C.; Shinde, S. K.; Patil, R. T.; Fulari, A. V.; Koli, R. R.; Kim, D. Y.; Lee, D. S.; Fulari, V. J. Structural and morphological changes in binder-free $MnCo_2O_4$ electrodes for supercapacitor applications: effect of deposition parameters. *J. Mater. Sci-Mater. El* **2019**, *30* (4), 3729−3743.
(21) Chen, H. Y.; Liu, Y. F.; Wu, R. Z.; Liu, X. H.; Liu, Y.; Xu, C. J. Battery-type and binder-free $MgCo_2O_4$-NWs@NF electrode materials for the assembly of advanced hybrid supercapacitors. *Int. J. Hydrogen Energ* **2022**, *47* (35), 15807−15819.
(22) Sun, J.; Du, X.; Wu, R.; Zhang, Y.; Xu, C.; Chen, H. Bundlelike $CuCo_2O_4$ Microstructures Assembled with Ultrathin Nanosheets As Battery-Type Electrode Materials for High-Performance Hybrid Supercapacitors. *Acs Appl. Energ Mater.* **2020**, *3* (8), 8026−8037.
(23) Wu, R. Z.; Sun, J. L.; Xu, C. J.; Chen, H. Y. $MgCo_2O_4$-based electrode materials for electrochemical energy storage and conversion: a comprehensive review. *Sustainable Energy & Fuels* **2021**, *5* (19), 4807−4829.
(24) Parayangattil Jyothibasu, J.; Chen, M. Z.; Lee, R. H. Polypyrrole/Carbon Nanotube Freestanding Electrode with Excellent Electrochemical Properties for High-Performance All-Solid-State Supercapacitors. *Acs Omega* **2020**, *5* (12), 6441−6451.
(25) Liu, Y.; Du, X.; Li, Y.; Bao, E.; Ren, X.; Chen, H.; Tian, X.; Xu, C. Nanosheet-assembled porous $MnCo_2O_{4.5}$ microflowers as electrode material for hybrid supercapacitors and lithium-ion batteries. *J. Colloid Interface Sci.* **2022**, *627*, 815−826.
(26) Bao, E.; Ren, X.; Wu, R.; Liu, X.; Chen, H.; Li, Y.; Xu, C. Porous $MgCo_2O_4$ nanoflakes serve as electrode materials for hybrid supercapacitors with excellent performance. *J. Colloid Interface Sci.* **2022**, *625*, 925−935.
(27) Wang, F. F.; Zhu, Y. F.; Tian, W.; Lv, X. B.; Zhang, H. L.; Hu, Z. F.; Zhang, Y. X.; Ji, J. Y.; Jiang, W. Co-doped Ni_3S_2@CNT arrays anchored on graphite foam with a hierarchical conductive network for high-performance supercapacitors and hydrogen evolution electrodes. *Journal of Materials Chemistry A* **2018**, *6* (22), 10490−10496.
(28) Saroha, R.; Khan, T. S.; Chandra, M.; Shukla, R.; Panwar, A. K.; Gupta, A.; Haider, M. A.; Basu, S.; Dhaka, R. S. Electrochemical Properties of Na(0.66)V(4)O(10) nanostructures as Cathode Material in Rechargeable Batteries for Energy Storage Applications. *Acs Omega* **2019**, *4* (6), 9878−9888.
(29) Zhu, L.; Chen, Z.; Song, Y.; Wang, P.; Jiang, Y.; Jiang, L.; Zhou, Y. N.; Hu, L. Lower ammoniation activation energy of CoN nanosheets by Mn doping with superior energy storage performance for secondary ion batteries. *Nanoscale* **2018**, *10* (12), 5581−5590.
(30) Alem, A. F.; Worku, A. K.; Ayele, D. W.; Wubieneh, T. A.; Teshager, A. A.; Tadele Mihret, K.; Admasu, B. T.; Teshager, M. A.; Asege, A. A.; Ambaw, M. D.; et al. Ag doped Co_3O_4 nanoparticles for high-performance supercapacitor application. *Heliyon* **2023**, *9* (2), No. e13286.
(31) Zare Asl, H.; Rozati, S. M. Electrochemical performance improvement of completely spray-deposited FTO/Zn-doped Co_3O_4 double layer thin films: Influence of Zn doping. *Chem. Phys. Lett.* **2023**, *815*, No. 140364.
(32) Peng, T.; Dai, X. H.; Zhang, Y. F.; Zheng, P. M.; Wang, J. Y.; Wang, S. H.; Wang, Z. L.; Zeng, Y. Y.; Li, J. C.; Jiang, H. Y. Facile synthesis of SiO_2@MnO_2 nanocomposites and their applications on platforms for sensitively sensing antibiotics and glutathione. *Sensor Actuat B-Chem.* **2020**, *304*, No. 127314.
(33) Min, X.; Guo, M.; Liu, L.; Li, L.; Gu, J. N.; Liang, J.; Chen, C.; Li, K.; Jia, J.; Sun, T. Synthesis of MnO_2 derived from spent lithium-ion batteries via advanced oxidation and its application in VOCs oxidation. *J. Hazard Mater.* **2021**, *406*, No. 124743.
(34) Shinde, S. K.; Jalak, M. B.; Kim, S. Y.; Yadav, H. M.; Ghodake, G. S.; Kadam, A. A.; Kim, D. Y. Effect of Mn doping on the chemical synthesis of interconnected nanoflakes-like CoS thin films for high performance supercapacitor applications. *Ceram. Int.* **2018**, *44* (18), 23102−23108.
(35) Zhang, Z. W.; Yin, L. W. Mn-doped $Co_2(OH)_3Cl$ xerogels with 3D interconnected mesoporous structures as lithium ion battery anodes with improved electrochemical performance. *Journal of Materials Chemistry A* **2015**, *3* (34), 17659−17668.
(36) Qin, C.; Wang, B.; Wang, Y. Metal-organic frameworks-derived Mn-doped Co_3O_4 porous nanosheets and enhanced CO sensing performance. *Sens. Actuators, B* **2022**, *351*, No. 130943.
(37) Kim, J. S.; Na, C. W.; Kwak, C. H.; Li, H. Y.; Yoon, J. W.; Kim, J. H.; Jeong, S. Y.; Lee, J. H. Humidity-Independent Gas Sensors Using Pr-Doped In_2O_3 Macroporous Spheres: Role of Cyclic Pr^{3+}/Pr^{4+} Redox Reactions in Suppression of Water-Poisoning Effect. *ACS Appl. Mater. Interfaces* **2019**, *11* (28), 25322−25329.
(38) Naveen, A. N.; Selladurai, S. Investigation on physiochemical properties of Mn substituted spinel cobalt oxide for supercapacitor applications. *Electrochim. Acta* **2014**, *125*, 404−414.
(39) Liu, S.; Nan, H.; Li, L.; Qin, T.; Cai, L.; Zhang, W.; Zheng, W. Unlocking the optimum supercapacitance of Co_3O_4 by reducing the Co valence state via Mn doping. *Mater. Today Commun.* **2021**, *28*, No. 102665.
(40) Liu, X.; Wang, M.; Wu, X. Tailoring Electrochemical Performance of Co_3O_4 Electrode Materials by Mn Doping. *Molecules* **2022**, *27* (21). DOI: 7344.
(41) Zhao, H.; Zhang, Z.; Zhou, C.; Zhang, H. Tuning the morphology and size of $NiMoO_4$ nanosheets anchored on $NiCo_2O_4$ nanowires: the optimized core-shell hybrid for high energy density asymmetric supercapacitors. *Appl. Surf. Sci.* **2021**, *541*, No. 148458.
(42) Dubal, D. P.; Chodankar, N. R.; Holze, R.; Kim, D. H.; Gomez-Romero, P. Ultrathin Mesoporous $RuCo_2O_4$ Nanoflakes: An Advanced Electrode for High-Performance Asymmetric Supercapacitors. *ChemSusChem* **2017**, *10* (8), 1771−1782.
(43) Kuang, L.; Ji, F.; Pan, X.; Wang, D.; Chen, X.; Jiang, D.; Zhang, Y.; Ding, B. Mesoporous $MnCo_2O_{4.5}$ nanoneedle arrays electrode for

high-performance asymmetric supercapacitor application. *Chemical Engineering Journal* **2017**, *315*, 491−499.
(44) Parveen, N.; Khan, Z.; Ansari, S. A.; Park, S.; Senthilkumar, S. T.; Kim, Y.; Ko, H.; Cho, M. H. Feasibility of using hollow double walled Mn_2O_3 nanocubes for hybrid Na-air battery. *Chemical Engineering Journal* **2019**, *360*, 415−422.
(45) Liu, S.; Yin, Y.; Ni, D.; Hui, K. S.; Ma, M.; Park, S.; Hui, K. N.; Ouyang, C.-Y.; Jun, S. C. New insight into the effect of fluorine doping and oxygen vacancies on electrochemical performance of Co_2MnO_4 for flexible quasi-solid-state asymmetric supercapacitors. *Energy Storage Materials* **2019**, *22*, 384−396.
(46) Li, G.; Chen, M.; Ouyang, Y.; Yao, D.; Lu, L.; Wang, L.; Xia, X.; Lei, W.; Chen, S.-M.; Mandler, D.; et al. Manganese doped Co_3O_4 mesoporous nanoneedle array for long cycle-stable supercapacitors. *Appl. Surf. Sci.* **2019**, *469*, 941−950.
(47) Liu, S.; Kang, L.; Zhang, J.; Jun, S. C.; Yamauchi, Y. Sodium preintercalation-induced oxygen-deficient hydrated potassium manganese oxide for high-energy flexible Mg-ion supercapacitors. *NPG Asia Mater.* **2023**, *15* (1), 9.
(48) Fu, Y.; He, H.; Li, X.; Wu, L.; Yan, R.; Zhang, J.; Xu, X.; Wang, F. Enhance supercapacitive performance of Ni foam electrode and $MnCo_2O_{4.5}$/Ni foam electrode. *Journal of Materials Science: Materials in Electronics* **2017**, *28* (2), 1562−1571.
(49) Xu, Y.; Wang, X.; An, C.; Wang, Y.; Jiao, L.; Yuan, H. Facile synthesis route of porous $MnCo_2O_4$ and $CoMn_2O_4$ nanowires and their excellent electrochemical properties in supercapacitors. *J. Mater. Chem. A* **2014**, *2* (39), 16480−16488.
(50) Prasath, A.; Athika, M.; Duraisamy, E.; Selva Sharma, A.; Sankar Devi, V.; Elumalai, P. Carbon Quantum Dot-Anchored Bismuth Oxide Composites as Potential Electrode for Lithium-Ion Battery and supercapacitor Applications. *Acs Omega* **2019**, *4* (3), 4943−4954.
(51) Esarev, I. V.; Agafonov, D. V.; Surovikin, Y. V.; Nesov, S. N.; Lavrenov, A. V. On the causes of non-linearity of galvanostatic charge curves of electrical double layer capacitors. *Electrochim. Acta* **2021**, *390*, No. 138896.
(52) Ambare, R. C.; Bharadwaj, S. R.; Lokhande, B. J. Electrochemical characterization of Mn: Co_3O_4 thin films prepared by spray pyrolysis via aqueous route. *Curr. Appl. Phys.* **2014**, *14* (11), 1582−1590.
(53) Karthikeyan, A.; Mariappan, R. Enhancing pseudo-capacitive behavior in Mn-doped Co3O4 nanostructures for supercapacitor applications. *J. Alloys Compd.* **2023**, *968*, No. 172094.
(54) Aslam, S.; Ramay, S. M.; Mahmood, A.; Mustafa, G. M.; Zawar, S.; Atiq, S. Electrochemical performance of transition metal doped Co_3O_4 as electrode material for supercapacitor applications. *J. Sol-Gel Sci. Technol.* **2023**, *105* (2), 360−369.
(55) Wang, S.; Zhang, L.; Sun, C.; Shao, Y.; Wu, Y.; Lv, J.; Hao, X. Gallium Nitride Crystals: Novel supercapacitor Electrode Materials. *Adv. Mater.* **2016**, *28* (19), 3768−3776.
(56) Li, S.; Wang, Y.; Sun, J.; Zhang, Y.; Xu, C.; Chen, H. Hydrothermal synthesis of Fe-doped Co_3O_4 urchin-like microstructures with superior electrochemical performances. *J. Alloys Compd.* **2020**, *821*, No. 153507.
(57) Aadil, M.; Nazik, G.; Zulfiqar, S.; Shakir, I.; Aboud, M. F. A.; Agboola, P. O.; Haider, S.; Warsi, M. F. Fabrication of nickel foam supported Cu-doped CoO nanostructures for electrochemical energy storage applications. *Ceram. Int.* **2021**, *47* (7), 9225−9233.
(58) Hao, P.; Zhao, Z.; Li, L.; Tuan, C. C.; Li, H.; Sang, Y.; Jiang, H.; Wong, C. P.; Liu, H. The hybrid nanostructure of $MnCo_2O_{4.5}$ nanoneedle/carbon aerogel for symmetric supercapacitors with high energy density. *Nanoscale* **2015**, *7* (34), 14401−14412.
(59) Maile, N. C.; Moztahida, M.; Ghani, A. A.; Hussain, M.; Tahir, K.; Kim, B.; Shinde, S. K.; Fulari, V. J.; Lee, D. S. Electrochemical synthesis of binder-free interconnected nanosheets of Mn-doped CoO on Ni foam for high-performance electrochemical energy storage application. *Chem. Eng. J.* **2021**, *421*, No. 129767.
(60) Liu, S. J.; Nan, H. S.; Li, L.; Qin, T. T.; Cai, L.; Zhang, W.; Zheng, W. T. Unlocking the optimum supercapacitance of CoO by reducing the Co valence state via Mn doping. *Mater. Today Commun.* **2021**, *28*, No. 102665.

https://doi.org/10.1021/acsomega.3c08650
ACS Omega 2024, 9, 6955−6964